minerals

MDPI

Article

Sm-Nd Dating and In-Situ LA-ICP-MS Trace Element Analyses of Scheelite from the Longshan Sb-Au Deposit, Xiangzhong Metallogenic Province, South China

Zhiyuan Zhang [1,2], Guiqing Xie [1,*], Jingwen Mao [1], Wengang Liu [3], Paul Olin [2] and Wei Li [1]

[1] MNR Key Laboratory of Metallogeny and Mineral Assessment, Institute of Mineral Resources, Chinese Academy of Geological Sciences, Beijing 100037, China; zhangzhiyuanstone@163.com (Z.Z.); jingwenmao@263.net (J.M.); liwei2012cugb@163.com (W.L.)

[2] Centre for Ore Deposit and Earth Sciences (CODES), University of Tasmania, Hobart, TAS 7001, Australia; paul.olin@utas.edu.au

[3] Tianjin Institute of Geology and Mineral Resources, Tianjin 300170, China; liuwg1988@163.com

* Correspondence: xieguiqing@cags.ac.cn

Received: 5 January 2019; Accepted: 28 January 2019; Published: 30 January 2019

Abstract: Longshan is an important Sb-Au ore deposit (3.7 Mt @4.5 wt. % Sb and 4.6 g/t Au) in the Xiangzhong metallogenic province (XZMP), South China. In the present work, trace element composition, Sm-Nd isotope dating, and Sr isotope of scheelite from the Longshan Sb-Au deposit are used to constrain the genesis of the deposit. Based on mineral assemblages and geological characteristics, two types of scheelites can be distinguished (Sch1 and Sch2). Sch1 is granular and cemented by stibnite, while Sch2 is commonly present in stibnite, pyrite, calcite, and quartz veins, indicating that Sch2 is later than Sch1. The Sm-Nd isochron age defined by Sch1 is 210 ± 2 Ma (MSWD = 1.0, n = 4). This age is interpreted as the age of Sb-Au mineralization and overlaps with the 201–228 Ma granitic rocks in the XZMP. Sch1 exhibits high ΣREE + Y contents (43.5 to 104 ppm), low Sr values (2687 to 6318 ppm, average of 4018 ppm), and a narrow range of $^{87}Sr/^{86}Sr$ values (0.7209 to 0.7210, average of 0.7209). In contrast, the elevated Sr abundance (4525 to 11,040 ppm, average of 6874 ppm) and wide $^{87}Sr/^{86}Sr$ ratios (0.7209 to 0.7228, average of 0.7214) in Sch2 were possibly caused by fluid-rock interaction mixing with Sr-enriched basement rocks. Sulfides have a narrow range of $\delta^{34}S$ values of −1.8‰ to 3.2‰, with an average value of 1.1‰ (n = 7). Geochronological, geochemical and isotopic data suggest that the Longshan Sb-Au deposit is possible genetically related to the Late Triassic granitic intrusion in the XZMP.

Keywords: scheelite; Sm-Nd dating; trace elements; Sb-Au deposit; Longshan

1. Introduction

Scheelite ($CaWO_4$) is a common accessory mineral that occurs in many gold deposits hosted by metamorphic rocks. However, the origin of these gold deposits continues to be debated, including a diversity of proposed genetic models (magmatic versus metamorphic) [1–6]. The Sm-Nd isotopes of scheelite can potentially be a powerful geochronometer for dating gold deposits [7–13]. Due to their similar electron configurations and ionic radii, elements such as rare earth elements (REEs), Sr and Y can substitute for Ca^{2+} in the scheelite structure [14,15]. Hence, scheelite contains abundant trace elements and REEs and has a high Sm/Nd ratio [7,16–18]. The REE composition of scheelite can provide information about the source and mineralization conditions of ore-forming fluids [4,15,19–21] as well as genetic types of deposits [22–24]. Scheelite lattice can accommodate limited Sr but rejects

Rb [25,26], and the radiogenic ^{87}Sr from ^{87}Rb has a negligible effect on Sr isotope composition. So, the scheelite Sr isotopic system can be used to trace the source of ore-forming fluids [3,7,12,27].

The Xiangzhong metallogenic province (XZMP), located at the eastern margin of the Yangtze Block, South China (Figure 1b), is one of the most important Sb-Au metallogenic domains in China [28,29]. Various interpretations have been proposed regarding the genesis of these deposits, including sedimentary exhalative processes based on the fact that chondrite-normalized REE patterns of the banded ores in Woxi W-Sb-Au deposit are similar with other SEDEX-type polymetallic ore deposits [30], orogenic-like processes since the characteristics of ore-forming fluids are in agreement with the definition of orogenic gold deposits [31], and intrusion-related deposit systems on account of sulfur and ore-forming fluids in these deposits were magmatic in origin [28]. This debate is mainly due to the lack of reliable mineralization ages in these Sb-Au deposits and to the absence of intrusion within the mining district [28].

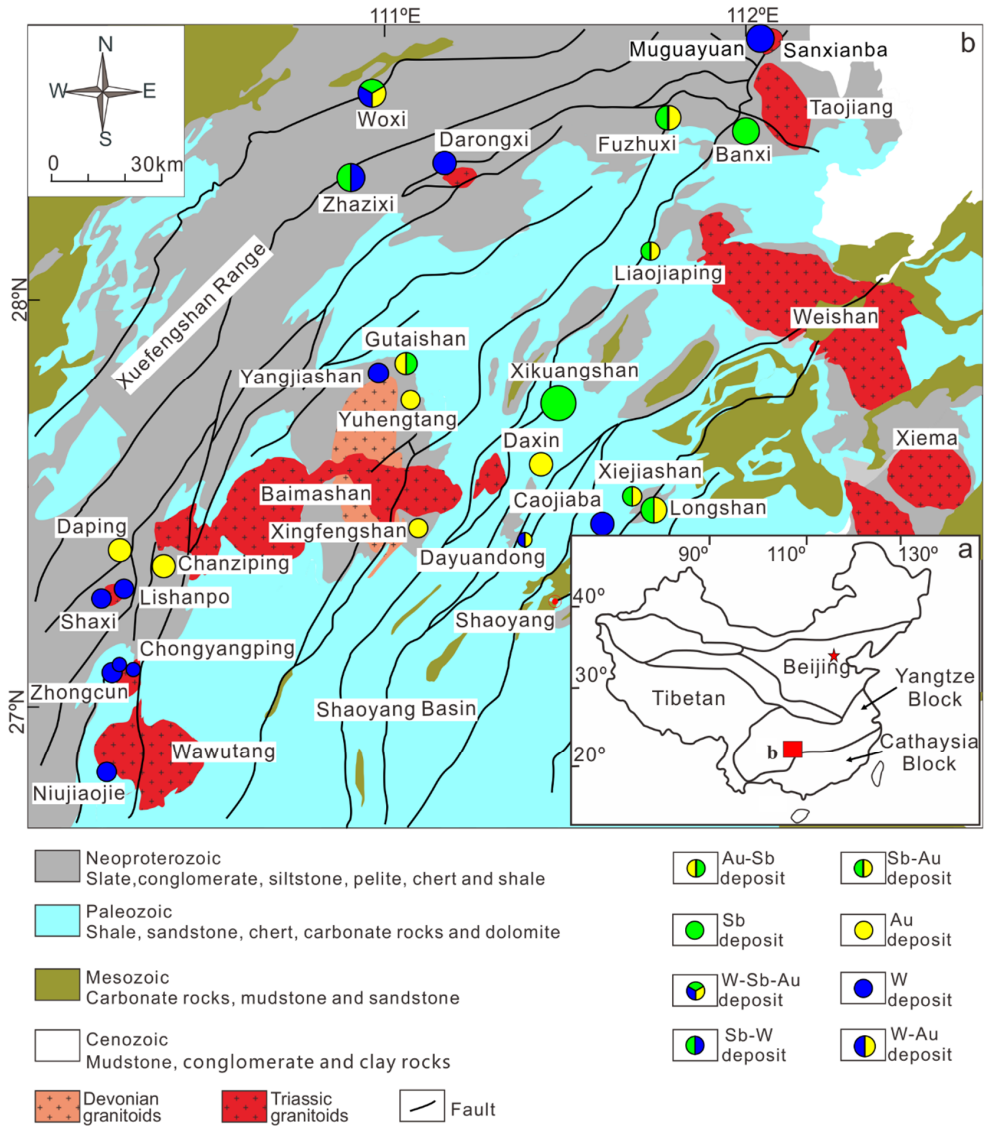

Figure 1. (**a**) Tectonic framework of China including the location of the XZMP. (**b**) Regional geological map of the XZMP in Central Hunan, South China, showing the distribution of granitic intrusions and important Sb, Au and W deposits (modified after Geological Map of the Hunan Province, the People's Republic of China [32]; Chu et al. [33]).

Longshan is an important Sb-Au deposit hosted by Neoproterozoic slates in the XZMP. Only two studies have constrained the chronology of the Longshan Sb-Au deposit. Quartz fluid inclusion Rb-Sr and pyrite Re-Os studies yielded isochron ages of 175 ± 27 Ma [34] and 195 ± 36 Ma [35], respectively, with large errors. The genesis of the Longshan Sb-Au deposit remains uncertain, particularly as the precise age and origin of the mineralization are not clear.

In this study, the in-situ trace element composition, Sm-Nd isotope dating, Sr isotopes of scheelite, and S isotopes of sulfides were carried out to constrain (1) the age of the Sb-Au mineralization and (2) the possible genetic relationship between the Sb-Au deposit and Late Triassic granitic intrusion in the XZMP.

2. Geological Setting

2.1. Regional Geology

South China consists of the Yangtze Block in the northwest and the Cathaysia Block in the southeast (Figure 1a, [36,37]). The XZMP, located at the eastern margin of the Yangtze Block [28], includes the Xuefengshan Range in the west and the Shaoyang Basin in the east (Figure 1b). Strata exposed in the XZMP consist mainly of Neoproterozoic metamorphic basement and Paleozoic to Cenozoic sedimentary rocks (Figure 1b). The Neoproterozoic rocks are part of the crystalline basement of South China and consist of slate, conglomerate, siltstone, pelite, chert, and shale. These basement rocks compose the majority of the wall rock for the Sb-Au and Au-Sb deposits [28,38].

In the XZMP, intrusive rocks are mostly observed to outcrop at the margins of the Shaoyang Basin and are dominated by Late Triassic granites and subordinate Devonian granitoids (Figure 1b, [33,39–42]. Numerous zircon SHRIMP and LA-ICP-MS U-Pb ages demonstrate that extensive Late Triassic granites were emplaced between 228 and 201 Ma in the XZMP [29]. Magmatic rocks are lacking in most of the Sb-Au deposit areas, although small felsic dikes are observed in some deposits. For example, mineralized veins cutting granite porphyries and quartz porphyries are observed in the Fuzhuxi and Liaojiaping Sb-Au deposits, and in the Banxi Sb deposit (Figure 1b, [28]). Moreover, Bouguer gravity and aeromagnetic anomalies suggest that hidden granitic intrusions may be present beneath the Longshan Sb-Au deposit [43].

More than 170 Sb-Au deposits have been discovered in the XZMP, hosted by Neoproterozoic clastic rocks and Devonian to Carboniferous carbonate rocks [44,45]. The Sb polymetallic deposits can be classified into two types, the Woxi-type and the Xikuangshan-type, based on ore-forming elements and host rocks [46]. The Woxi-type deposits contain a W-Sb-Au metal association and, in some cases, Sb-W mineralization, and is represented by the Zhazixi deposit [12,47–50]. These deposits are hosted by Proterozoic low-grade metamorphosed clastic rocks. The Xikuangshan-type deposits in the Shaoyang Basin are hosted by Devonian-Carboniferous limestone-sandstones and characterized by Sb mineralization [51].

2.2. Deposit Geology

The Longshan Sb-Au deposit is located in the central part of the so-called "Longshan dome" (Figure 2). The dome is made up of Neoproterozoic slates. Cambrian to Ordovician shales are distributed around the dome in a ring belt, and Devonian to Carboniferous siltstone and mudstone are distributed along the east and west sides of the Longshan dome (Figure 2). Late Triassic granitic dikes are developed around the eastern part of the dome (Figure 2), and the zircon U-Pb ages (220–217 Ma, [52]) are consistent with those of the Late Triassic granites formed in the XZMP [29].

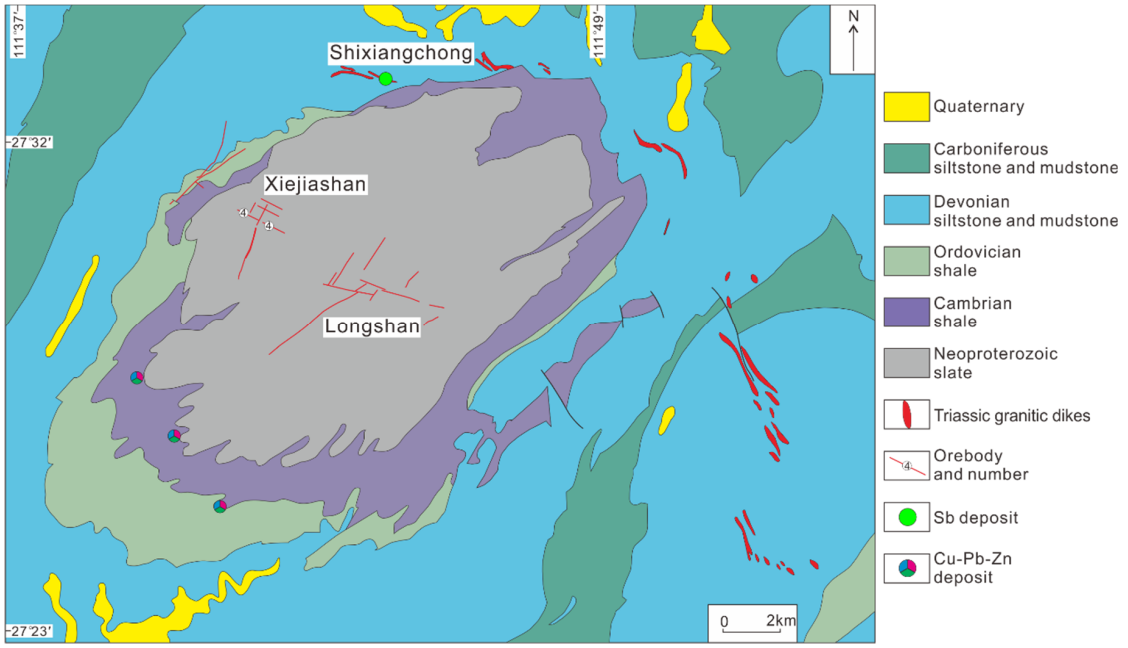

Figure 2. Simplified geological map of Longshan dome, South China (modified after Chen et al. [52]).

The Longshan Sb-Au deposit (3.7 Mt @4.5 wt. % Sb and 4.6 g/t Au, [53]) contains two mining zones: Longshan and Xiejiashan (Figure 2). These include 27 NE-striking, NWW-striking and NNE-striking vein groups. The No.1 and No.2 vein groups (Figure 3a), which are the largest ore bodies, occur as a steeply NWW-striking and NE-dipping (65–80°) body within metamorphic slates. It is more than 1400 m long and 0.2 to 1.3 m wide and continues for 1050 m down-dip, with an average grade of 0.77 to 6.79 wt. % Sb and 0.3 to 4.6 g/t Au.

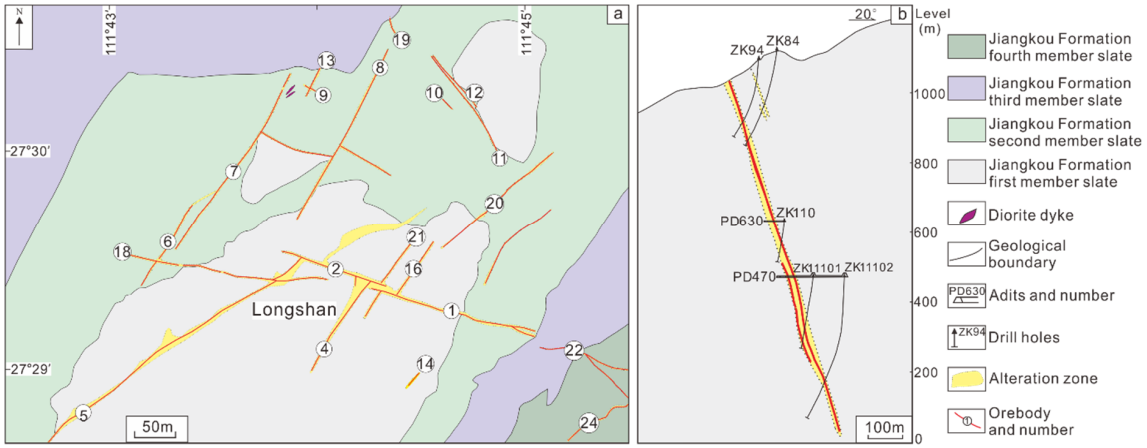

Figure 3. (**a**) Simplified geological map of the Longshan mining district in Longshan deposit, South China; (**b**) cross–section map of the Longshan mining district in Longshan deposit, South China (modified after Hunan Bureau of Geology and Mineral Resources [53]).

Diorite dikes occurred on the northwest side of the Longshan mining zone (Figure 3a), however, we were unable to collect the sample due to a lack of outcrop. The Longshan deposit is underlain by rocks of the Neoproterozoic Jiangkou Formation containing a series of low-grade metamorphic slates. The Jiangkou Formation can be further divided into four members from bottom to top (Figure 3). The first and second members consist of pebbly sandy slate and tuffaceous pebbly sandy slate, and the orebodies mainly occur in the two members. The third and fourth members consist of dark-gray and gray-green pebbly sandy slate (Figure 3).

Wallrock alteration in the Longshan deposit is pervasive and is best developed adjacent to quartz veins. The scale and intensity of alteration show a correlation with the width of the quartz veins. Alteration styles include sulfidation, silicification, sericitization, and carbonatization (Figure 4). Sulfidation is caused by the presence of arsenopyrite and pyrite.

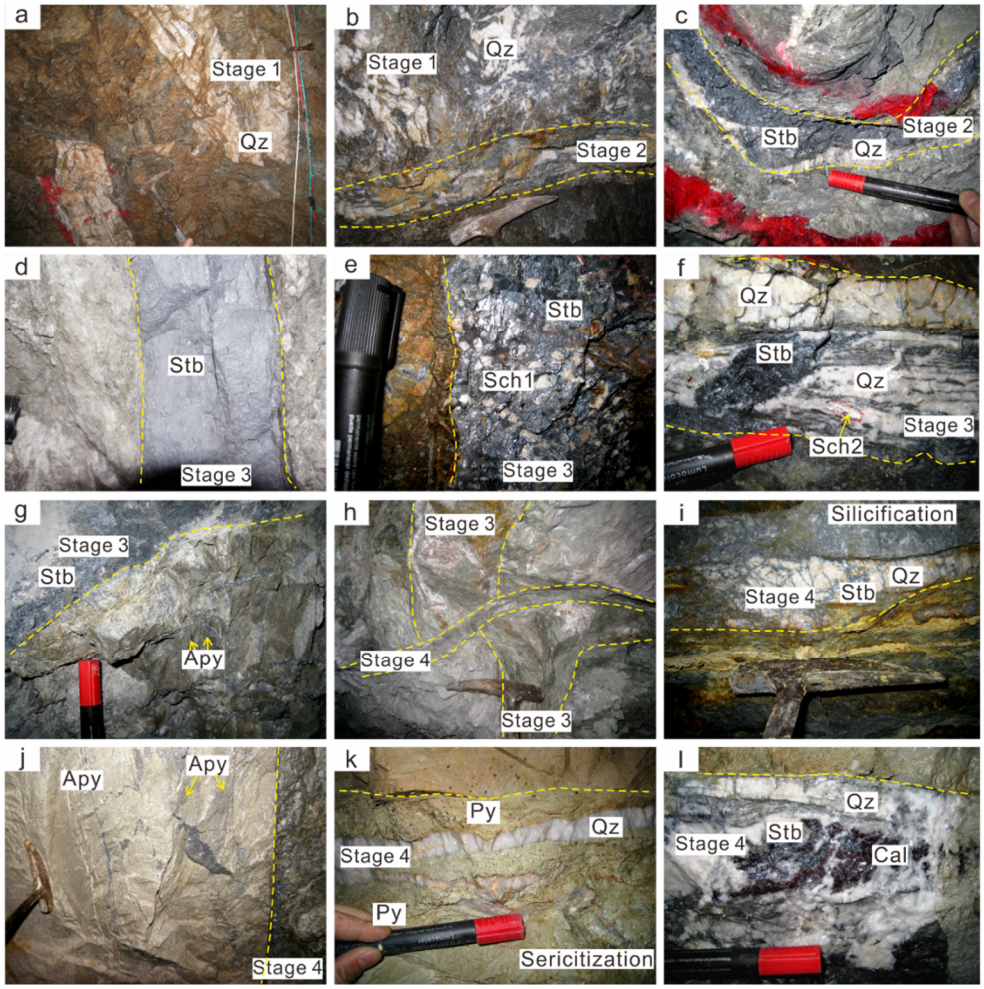

Figure 4. Field occurrences of mineralization and alteration in the Longshan Sb-Au deposit. (**a**) Deformed Stage-1 quartz veins occur as irregular veins within Jiangkou Formation; (**b**) Stage-2 quartz-sulfide veins cut the Stage-1 quartz veins, with distinct boundaries; (**c**) Quartz and stibnite from the Stage-2 show intense deformation; (**d**) View of the Stage-3 fine-grained stibnite vein within Jiangkou Formation; (**e**) Stage-3 fine-grained Sch1 scheelite cemented by stibnite; (**f**) Stage-3 quartz-stibnite mineralization associated with Sch2 scheelite; (**g**) Fine-grained arsenopyrite and quartz-stibnite veinlets developed proximal to the Stage-3 stibnite vein; (**h**) Crosscutting relationship between Stage-3 and Stage-4 quartz veins; (**i**) Stage-4 intense host rock silicification through a network of veins defining a brecciated host-rock and the intergrowth of quartz and stibnite; (**j**) Fine-grained, sparsely disseminated arsenopyrite developed proximally to the Stage-4 ore veins in the country rocks; (**k**) Coarse-grained, densely disseminated pyrite developed intensively in the wallrock close to the Stage-4 quartz vein, note the abundance of sericitization within the discolored wallrock; (**l**) Stage-4 assemblage of stibnite and calcite in the quartz vein. Qz = quartz; Stb = stibnite; Sch = scheelite; Apy = arsenopyrite; Py = pyrite; Cal = calcite.

Based on field and microscopic observations, we recognized a mineral paragenesis, including four distinct stages accompanied by varying degrees of alteration (Figure 5). The pre-mineralization Stage-1 is represented by deformed segregation quartz veins that are several to tens of cm in thickness

(Figure 4a). Stage-2 is marked by NE-striking and NW-dipping quartz-sulfide veins with widths of 1 to 20 cm. The quartz-sulfide veins cut the Stage-1 quartz veins, with distinct boundaries (Figure 4b). The veins mainly comprise galena, quartz, stibnite, and pyrite (Figures 4c and 6a,b). Minor chalcopyrite associated with sphalerite and pyrrhotite occur in the ores (Figure 7a). The wallrock alteration including sulfidation and silicification is weak in this stage. Stage-3 represents the main stibnite and gold mineralization stage, which is marked by NWW-striking and NE-dipping quartz-sulfide veins with widths of 0.2 to 1.4 m (Figure 4d–f). High-grade stibnite ore (Figure 6d) is infilled with native gold (Figure 7f). Pyrite infilled with native gold (Figure 7e) is associated with stibnite (Figure 6e) and jamesonite (Figure 7g). Arsenopyrite developed proximally to the stibnite vein (Figure 4g). Stage-4 is marked by NNE-striking and NW-dipping quartz-sulfide veins, from 0.1 to 0.68 m in width (Figure 4i–l), locally cutting the Stage-3 quartz veins (Figure 4h). Coarse-grained disseminated arsenopyrite and pyrite (Figure 4j,k and Figure 6f) are developed in the wallrock during Stage-4; meanwhile, abundant sericitization (Figure 4k) occurs within the discolored wallrock. Arsenopyrite replaced by chalcostibite (Figure 7h) or native antimony (Figure 7i) is observed. The local development of an assemblage of calcite and stibnite (Figure 4l) occurs in the quartz vein.

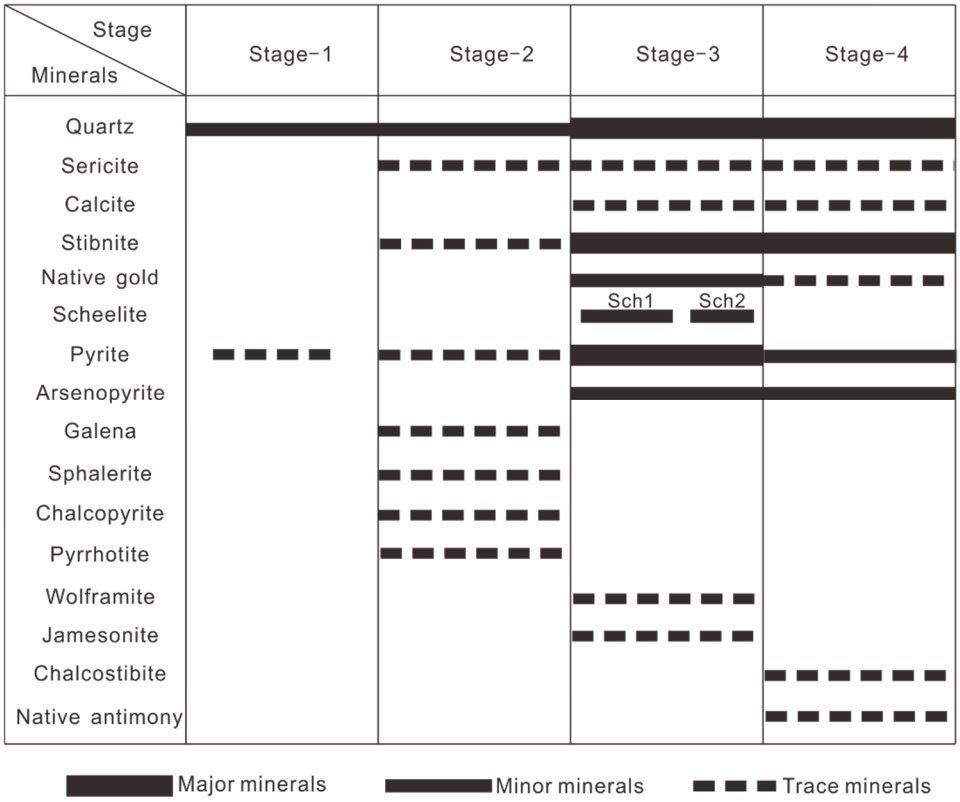

Figure 5. Paragenesis of the mineral assemblages showing the mineralized sequence of the Longshan Sb-Au deposit, South China. Line thickness indicates approximate relative mineral abundance.

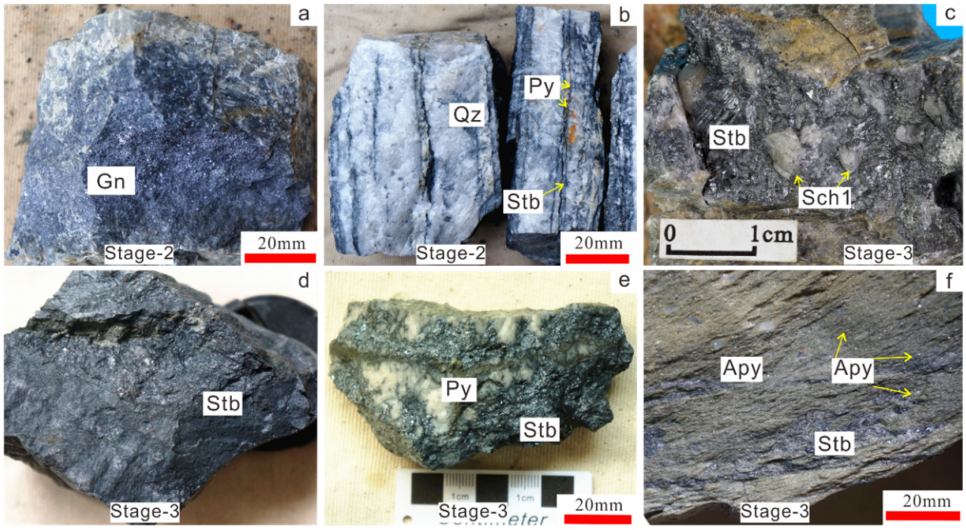

Figure 6. Representative photographs of samples selected for ore mineralogy. (**a**) Stage-2 galenite ore; (**b**) Stage-2 quartz-stibnite-pyrite ore containing coarse-grained pyrite; (**c**) Stage-3 coarse-grained Sch1 scheelite cemented by euhedral-subhedral stibnite; (**d**) Stage-3 high grade stibnite ore; (**e**) Stage-3 pyrite veinlet associated with stibnite; (**f**) Stage-4 arsenopyrite densely disseminated in the wallrock. Gn = galena; Qz = quartz; Py = pyrite; Stb = stibnite; Sch1 = scheelite type1; Apy = arsenopyrite.

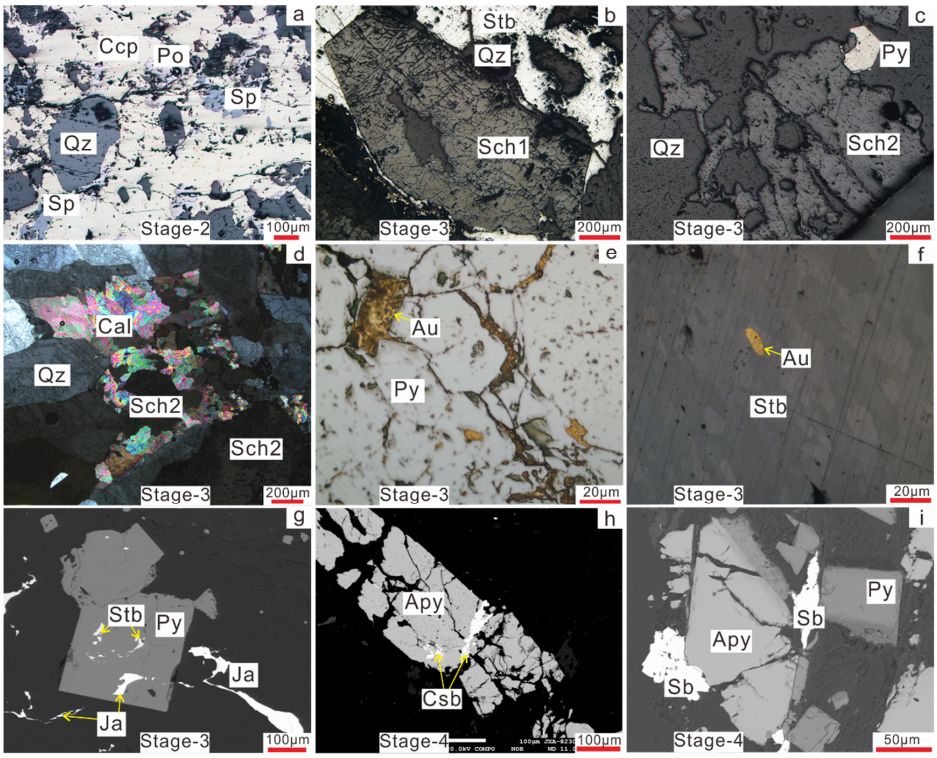

Figure 7. Typical photomicrographs of the Longshan Sb-Au deposit. (**a**) Stage-2 chalcopyrite associated with sphalerite and pyrrhotite; (**b**) Stage-3 euhedral Sch1 scheelite cemented by stibnite; (**c**) Stage-3 Sch2 scheelite associated with pyrite; (**d**) Stage-3 Sch2 coexisted with calcite and quartz; (**e**) Stage-3 native gold associated with euhedral-subhedral pyrite; (**f**) Stage-3 native gold associated with stibnite; (**g**) Stage-3 Pyrite associated with stibnite and jamesonite; (**h**) Stage-4 euhedral-subhedral arsenopyrite replaced by chalcostibite; (**i**) Stage-4 euhedral arsenopyrite replaced by native antimony. Sp = sphalerite; Ccp = chalcopyrite; Po = pyrrhotite; Qz = quartz; Stb = stibnite; Sch1 = scheelite type1; Sch2 = scheelite type2; Py = pyrite; Cal = calcite; Au = native gold; Ja = Jamesonite; Csb = chalcostibite; Sb = native antimony; Apy = arsenopyrite.

The scheelite is well formed in Stage-3 and can be divided into two types. Coarse-grained Sch1 is coexisted with stibnite and quartz (Figures 6c and 7b). Sch2 is commonly present in pyrite, calcite and quartz veins (Figure 4f) and is associated with pyrite (Figure 7c) and calcite (Figure 7d). The different mineral assemblages indicate that Sch2 is later than Sch1.

3. Sample Descriptions and Analytical Methods

3.1. Sample Descriptions

More than 120 hand-specimen samples, representative of all stages and mineralization styles, were collected from Longshan deposit. Eighteen scheelite and sulfide samples (Table S1) collected from underground adits at the +298 m to +720 m levels, were investigated in this study. The scheelite grains were separated for dating using conventional heavy liquid and magnetic techniques. Standard petrographic thin-sections were prepared from scheelite and sulfide samples for optical microscopy to identify mineral paragenetic relationships. Backscattered electron (BSE), scanning electron microscopy (SEM) and cathodoluminescence (CL) images (Figure 8) were obtained using a Hitachi SU-70 analytical field emission scanning electron microscope (Hitachi, Ltd., Chiyoda, Japan) at the University of Tasmania (UTAS), Australia.

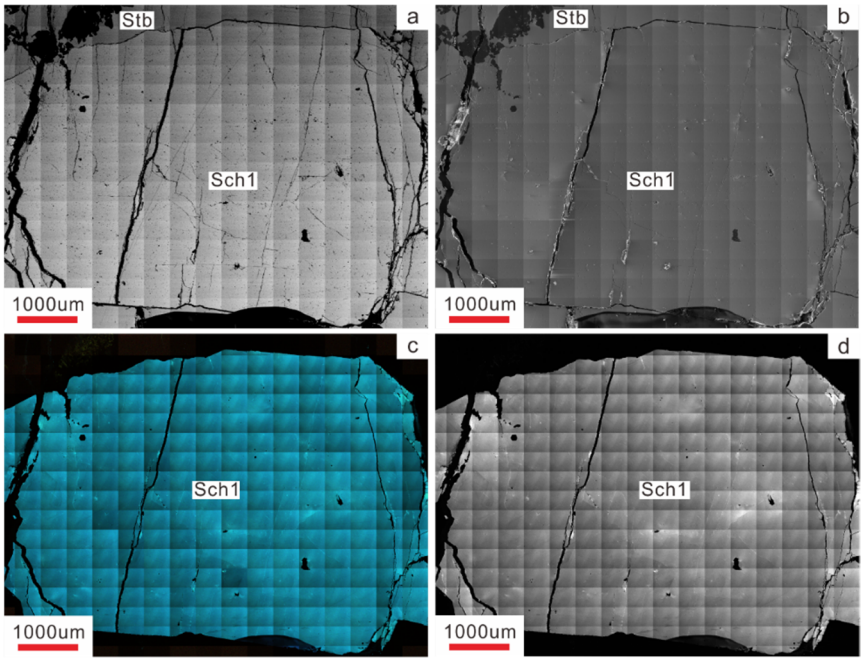

Figure 8. The (**a**) Backscattered electron (BSE) image; (**b**) Scanning Electron Microscopy (SEM) image; (**c**) Colorful Cathodoluminescence (CL) image; and (**d**) Grey Cathodoluminescence (CL) image of the Sch1 from the Longshan Sb-Au deposit indicate that its chemical composition is homogeneous.

3.2. Trace Element

Each sample was prepared as a 1-inch-diameter polished mount. Quantitative LA-ICP-MS trace element analyses of scheelite from the Longshan Sb-Au deposit was analyzed using a Resonetics Resolution laser ablation system equipped with a Coherent COMPex Pro 110 ArF Excimer laser (Coherent, Inc., Santa Clara, CA, USA) operating at a 193-nm wavelength with a 20-ns pulse width. The laser is coupled to an Agilent 7700 quadrupole inductively-coupled plasma mass spectrometer (ICP-MS) housed at CODES Analytical Laboratories, UTAS. All scheelite samples were ablated on 51 μm diameter spots using the laser at 10 Hz and an energy of density of 2.7 J/cm^2. Each analysis was pre-ablated with five laser pulses to remove the surface contamination. Once the pre-ablation had washed out (20 s), a blank gas was analyzed for 30 s followed by 60 s of sample ablation for scheelite.

All data reduction calculations and error propagations were undertaken within the software LADR designed at CODES analytical laboratories, UTAS. Data reduction was undertaken using stoichiometric values of Ca as the internal standard for scheelite. Glass standard NIST612 was measured using a 74 μm spot size (10 Hz, 3.5 J/cm^2) as the primary calibration standard. Since the low content of rare earths in NIST612 in comparing with the studied mineral, we chose different laser sizes for the analysis of standards and scheelite. GSD-1G and BCR-2 (51 μm, 10 Hz, 3 J/cm^2) were used as the secondary standards. Standard standard and unknowns analyses were used to compare values for each element and to correct for differences in spot size between the primary. Measured isotopes and detection limits are given in Table S2.

3.3. Sm-Nd and Sr Isotope

Based on field investigations and microscopic observations, scheelite chips were cut from hand specimens and lightly crushed to a size of 40 to 60 mesh. Scheelite was prepared using standard heavy liquid methods, with final purification achieved by handpicking under a binocular microscope with the aid of a UV lamp. The cleaned fractions, with a purity of 99%, were powdered to ~74 μm in an agate mortar. Approximately 50 mg of scheelite samples was dissolved in Teflon bombs using a mixture of acid solution (2 mL 22 M HF + 1 mL 15 M HNO_3 + 0.5 mL concentrated $HClO_4$). Two separate sample aliquots were dissolved: one for the determination of present-day $^{87}Sr/^{86}Sr$ and $^{l43}Nd/^{144}Nd$ ratios and the other for spiking with ^{149}Sm-^{146}Nd spike and determination of Sm and Nd concentrations. The bombs were placed in an oven at 190 °C for two days. After drying on a hot plate at 150 °C, 3 mL 6 M HCl was added and evaporated to dryness again. Finally, the samples were dissolved with 1 mL 2.5 M HCl. The solution was centrifuged, and the supernatant liquid was loaded onto the preconditioned resin column with 2 mL of AG50W × 12 (200–400 mesh) for the separation of Sr and LREE from the sample matrix. Sm and Nd were separated by HEHEHP chromatographic columns. Isotope analyses were performed by thermal ionization mass spectrometry (TIMS) using a Triton instrument from Thermo Fisher Scientific at the Tianjin Institute of Geology and Mineral Resources. Sr isotopic ratios were normalized to an $^{86}Sr/^{88}Sr$ ratio of 0.1194, and Nd isotope ratios were normalized to a $^{146}Nd/^{144}Nd$ ratio of 0.7219. The reproducibility of the isotopic ratios was approximately 0.003% at the 2σ level, and the precisions for the Nd and Sm concentrations at the 2σ level were approximately ± 0.5% of the quoted values. Concentrations for the rock standard USGS BCR-2 determined during this study were 6.58 ppm Sm and 28.92 ppm Nd. BCR-2 was used to evaluate the separation and purification process of Nd and yielded $^{143}Nd/^{144}Nd$=0.512636 ± 0.000006, which was consistent with the reference value of 0.512634 ± 0.000012 [54]. The NBS987 standard yielded an $^{87}Sr/^{86}Sr$ value of 0.710245 ± 0.000025 (2σ, n = 10); and the JMC Nd standard provided a $^{l43}Nd/^{144}Nd$ value of 0.511132 ± 0.000020 (2σ, n = 10). Blanks during this study were 30 pg for Sm, 54 pg for Nd, and 0.56 ng for Sr and Rb. The Sm-Nd isochron age was calculated using the ISOPLOT plotting program [55]. In this study, the decay constant λ used for ^{147}Sm was 6.54 × 10^{-12} a^{-1}, and the $^{147}Sm/^{144}Nd$ and $^{143}Nd/^{144}Nd$ values of the chondritic uniform reservoir (CHUR) used for the εNd(t) calculations were 0.1967 and 0.512638 [56], respectively.

3.4. Sulfur Isotopes

Arsenopyrite and pyrite grains were carefully handpicked under a binocular microscope after the samples had been crushed and sieved to a size of 60 to 80 mesh with a purity of 99%. The sulfur isotope analyses of seven sulfide samples were performed on the SO_2 gas extracted from pyrite using conventional methods. Sulfide was mixed with Cu_2O in a 1:10 proportion and heated under vacuum (2.0 × 10^{-2} Pa) at 980 °C to release SO_2, after which the sulfur isotope ratios were measured using a MAT-251 mass spectrometer. The analytical precision was better than ± 0.2‰, relative to the Vienna Canon Diablo Troilite (V-CDT) sulfide.

4. Analytical Results

4.1. Trace Element Concentration in Scheelite

A total of 38 LA-ICP-MS REE analyses were carried out on four samples of scheelite from the Longshan Sb-Au deposit, and the results are presented in Tables 1 and 2. Sch1 exhibits high REE and Y contents with ΣREE + Y abundances ranging from 43.5 to 104 ppm. The REE_N distribution patterns of Sch1 (Figure 9a,b) are similar, with a positive "hump" in the MREE. However, Sch2 exhibits low REE and Y contents with ΣREE + Y abundances ranging from 0.349 to 25.1 ppm. The REE_N distribution patterns of Sch2 (Figure 9c,d) are similar, with depletions in the LREE.

Table 1. REE and trace element compositions (ppm) of scheelite from the Longshan Sb-Au deposit, South China.

Type	Sample No.	La	Ce	Pr	Nd	Sm	Eu	Gd	Tb	Dy	Ho	Er	Tm
Sch1	XJS-22-1	3.34	7.88	1.29	7.29	3.95	1.89	5.36	0.773	4.24	0.687	1.61	0.191
Sch1	XJS-22-2	2.20	5.30	0.832	4.58	2.28	1.22	3.10	0.458	2.56	0.410	0.987	0.126
Sch1	XJS-22-3	2.93	6.89	1.13	6.27	3.08	1.66	4.33	0.628	3.51	0.559	1.36	0.162
Sch1	XJS-22-4	2.80	7.07	1.25	7.23	3.91	2.11	5.66	0.793	4.31	0.684	1.54	0.167
Sch1	XJS-22-5	3.22	7.95	1.33	7.61	4.07	2.16	5.54	0.811	4.31	0.680	1.57	0.187
Sch1	XJS-22-6	3.40	8.95	1.55	9.29	5.18	2.55	7.08	1.03	5.44	0.838	1.89	0.225
Sch1	XJS-22-7	3.95	11.2	2.02	11.8	6.65	3.41	8.97	1.28	6.87	1.05	2.36	0.277
Sch1	XJS-22-8	3.13	9.07	1.78	11.4	7.50	3.40	9.96	1.37	6.89	1.00	2.12	0.233
Sch1	XJS-22-9	2.32	6.09	1.03	5.78	2.89	1.40	3.49	0.504	2.65	0.439	1.06	0.141
Sch1	XJS-22-10	5.21	12.2	1.98	10.8	5.64	2.83	7.46	1.14	6.40	1.07	2.60	0.315
Sch1	XJS-28-1	3.07	8.35	1.29	6.62	3.55	1.69	5.68	0.991	5.45	0.850	1.83	0.209
Sch1	XJS-28-2	2.69	7.19	1.16	6.10	3.33	1.51	5.27	0.911	4.88	0.736	1.61	0.177
Sch1	XJS-28-3	3.10	7.70	1.17	6.01	3.30	1.68	5.34	0.978	5.56	0.900	2.05	0.239
Sch1	XJS-28-4	2.59	6.29	0.964	4.86	2.55	1.20	4.08	0.767	4.74	0.754	1.79	0.208
Sch1	XJS-28-5	2.89	7.24	1.16	6.13	3.67	1.74	6.36	1.10	5.78	0.825	1.64	0.177
Sch1	XJS-28-6	3.23	7.89	1.20	6.13	3.47	1.63	5.69	1.07	6.16	0.951	2.20	0.249
Sch1	XJS-28-7	2.07	5.57	0.875	4.52	2.87	1.42	4.92	0.847	4.45	0.638	1.29	0.125
Sch1	XJS-28-8	3.65	9.25	1.49	8.08	4.72	2.28	8.24	1.46	7.81	1.13	2.27	0.229
Sch1	XJS-28-9	4.06	10.2	1.56	8.00	4.15	1.96	6.97	1.33	7.89	1.26	2.90	0.312
Sch1	XJS-28-10	4.16	10.9	1.80	9.76	5.54	2.62	9.55	1.69	9.65	1.42	3.01	0.304
Sch1	XJS-28-11	2.80	6.75	1.01	5.29	3.01	1.48	5.35	0.957	5.06	0.688	1.41	0.148
Sch2	XJS-36-1	0.162	0.350	0.051	0.337	0.355	0.328	0.996	0.187	1.33	0.267	0.956	0.173
Sch2	XJS-36-2	0.104	0.341	0.069	0.436	0.439	0.341	1.02	0.198	1.43	0.281	0.901	0.133
Sch2	XJS-36-3	0.064	0.144	0.018	0.087	0.076	0.072	0.197	0.046	0.416	0.098	0.371	0.066
Sch2	XJS-36-4	0.061	0.143	0.031	0.281	0.342	0.193	0.690	0.120	0.701	0.127	0.364	0.064
Sch2	XJS-36-5	0.146	0.411	0.057	0.353	0.298	0.213	0.672	0.149	1.09	0.230	0.799	0.144
Sch2	XJS-36-6	0.050	0.085	0.009	0.040	0.033	0.035	0.070	0.020	0.177	0.052	0.219	0.049
Sch2	XJS-36-7	0.190	0.534	0.059	0.235	0.089	0.156	0.275	0.067	0.711	0.187	0.728	0.145
Sch2	XJS-70-1	0.009	0.011	0.001	0.007	0.005	0.011	0.022	0.006	0.065	0.011	0.039	0.007
Sch2	XJS-70-2	0.063	0.117	0.013	0.057	0.056	0.039	0.216	0.046	0.346	0.064	0.207	0.029
Sch2	XJS-70-3	0.021	0.031	0.002	0.007	0.008	0.014	0.061	0.016	0.140	0.033	0.120	0.023
Sch2	XJS-70-4	0.002	0.010	0.001	0.003	0.009	0.008	0.051	0.011	0.077	0.014	0.052	0.006
Sch2	XJS-70-5	0.003	0.009	0.002	0.006	0.005	0.012	0.051	0.016	0.121	0.023	0.069	0.010
Sch2	XJS-70-6	0.021	0.034	0.003	0.040	0.064	0.063	0.220	0.041	0.259	0.052	0.151	0.024
Sch2	XJS-70-7	0.006	0.009	0.001	0.004	0.006	0.008	0.016	0.003	0.022	0.004	0.013	0.002
Sch2	XJS-70-8	0.005	0.009	0.001	0.003	0.004	0.009	0.020	0.003	0.017	0.004	0.018	0.003
Sch2	XJS-70-9	0.026	0.034	0.003	0.024	0.017	0.029	0.114	0.012	0.123	0.020	0.085	0.011
Sch2	XJS-70-10	0.051	0.047	0.006	0.019	0.021	0.020	0.088	0.019	0.093	0.031	0.120	0.026

Table 2. REE and trace element compositions (ppm) of scheelite from the Longshan Sb-Au deposit, South China.

Type	Sample No.	Yb	Lu	Y	LREE	MREE	HREE	REE	∑REE + Y	Na	Sr	Mo
Sch1	XJS-22-1	1.03	0.082	27.2	19.8	16.2	3.60	39.6	66.9	1.06	3688	0.014
Sch1	XJS-22-2	0.705	0.064	18.7	12.9	9.60	2.29	24.8	43.5	1.31	2687	0.013
Sch1	XJS-22-3	0.869	0.08	24.0	17.2	13.2	3.03	33.5	57.4	0.586	3623	0.011
Sch1	XJS-22-4	0.965	0.081	26.8	18.4	16.8	3.44	38.6	65.4	0.80	4044	0.009
Sch1	XJS-22-5	1.01	0.085	28.9	20.1	16.9	3.53	40.5	69.4	bdl	4633	0.005
Sch1	XJS-22-6	1.24	0.101	33.0	23.2	21.3	4.29	48.7	81.7	0.79	4332	0.004
Sch1	XJS-22-7	1.56	0.132	42.7	29.0	27.2	5.39	61.6	104	1.07	3724	0.012
Sch1	XJS-22-8	1.20	0.101	34.4	25.4	29.1	4.66	59.2	93.6	1.12	3835	0.016
Sch1	XJS-22-9	0.812	0.077	19.5	15.2	10.9	2.53	28.7	48.2	0.93	2982	0.006
Sch1	XJS-22-10	1.80	0.161	44.6	30.2	23.5	5.94	59.6	104	1.11	5946	0.013
Sch1	XJS-28-1	1.08	0.09	27.9	19.3	17.4	4.06	40.8	68.6	1.48	3500	0.010
Sch1	XJS-28-2	0.941	0.075	24.2	17.1	15.9	3.54	36.6	60.7	bdl	3800	0.006
Sch1	XJS-28-3	1.20	0.105	31.5	18.0	16.9	4.50	39.3	70.8	bdl	6318	0.008
Sch1	XJS-28-4	1.13	0.090	26.7	14.7	13.3	3.97	32.0	58.7	1.03	3975	0.015
Sch1	XJS-28-5	0.894	0.070	26.1	17.4	18.7	3.61	39.7	65.8	0.594	4156	0.011
Sch1	XJS-28-6	1.31	0.112	31.9	18.5	18.0	4.82	41.3	73.2	0.60	4029	0.008
Sch1	XJS-28-7	0.666	0.054	20.5	13.0	14.5	2.77	30.3	50.8	0.785	2786	0.010
Sch1	XJS-28-8	1.19	0.097	34.5	22.5	24.5	4.91	51.9	86.4	0.611	4106	0.007
Sch1	XJS-28-9	1.72	0.128	40.0	23.8	22.3	6.32	52.5	92.5	0.711	4222	0.007
Sch1	XJS-28-10	1.56	0.136	41.9	26.6	29.0	6.43	62.0	104	1.64	4280	0.017
Sch1	XJS-28-11	0.759	0.057	22.6	15.8	15.9	3.07	34.8	57.3	0.752	3708	0.009
Sch2	XJS-36-1	1.35	0.168	18.1	0.90	3.19	2.91	7.0	25.1	3.63	5296	0.098
Sch2	XJS-36-2	0.943	0.094	13.1	0.95	3.43	2.35	6.74	19.9	6.76	4694	0.648
Sch2	XJS-36-3	0.572	0.081	6.73	0.314	0.807	1.19	2.31	9.04	1.06	10,111	0.023
Sch2	XJS-36-4	0.605	0.079	6.35	0.516	2.05	1.24	3.80	10.2	3.96	5589	0.152
Sch2	XJS-36-5	0.994	0.113	11.0	0.967	2.43	2.28	5.67	16.7	13.1	7213	0.311
Sch2	XJS-36-6	0.452	0.062	4.24	0.184	0.336	0.833	1.35	5.59	4.53	4553	0.014
Sch2	XJS-36-7	1.24	0.175	11.8	1.02	1.30	2.47	4.79	16.6	3.92	6326	0.057
Sch2	XJS-70-1	0.055	0.005	0.618	0.027	0.109	0.117	0.254	0.872	3.03	7370	0.016
Sch2	XJS-70-2	0.153	0.02	2.69	0.251	0.703	0.473	1.43	4.12	5.06	6936	0.233
Sch2	XJS-70-3	0.155	0.025	1.84	0.061	0.239	0.356	0.656	2.50	8.30	10,025	0.015
Sch2	XJS-70-4	0.043	0.004	0.656	0.016	0.157	0.119	0.292	0.947	4.98	10,203	0.026
Sch2	XJS-70-5	0.053	0.007	0.942	0.020	0.206	0.163	0.389	1.33	1.84	11,040	0.018
Sch2	XJS-70-6	0.156	0.021	2.08	0.098	0.646	0.404	1.15	3.22	2.93	5274	0.214
Sch2	XJS-70-7	0.020	0.004	0.306	0.020	0.056	0.043	0.119	0.425	bdl	6493	0.09
Sch2	XJS-70-8	0.012	0.004	0.238	0.018	0.052	0.040	0.110	0.349	3.99	5984	0.113
Sch2	XJS-70-9	0.085	0.014	1.28	0.087	0.295	0.214	0.595	1.88	5.12	5226	0.35
Sch2	XJS-70-10	0.305	0.044	2.70	0.122	0.241	0.526	0.889	3.59	bdl	4525	0.186

bdl = below detection limit.

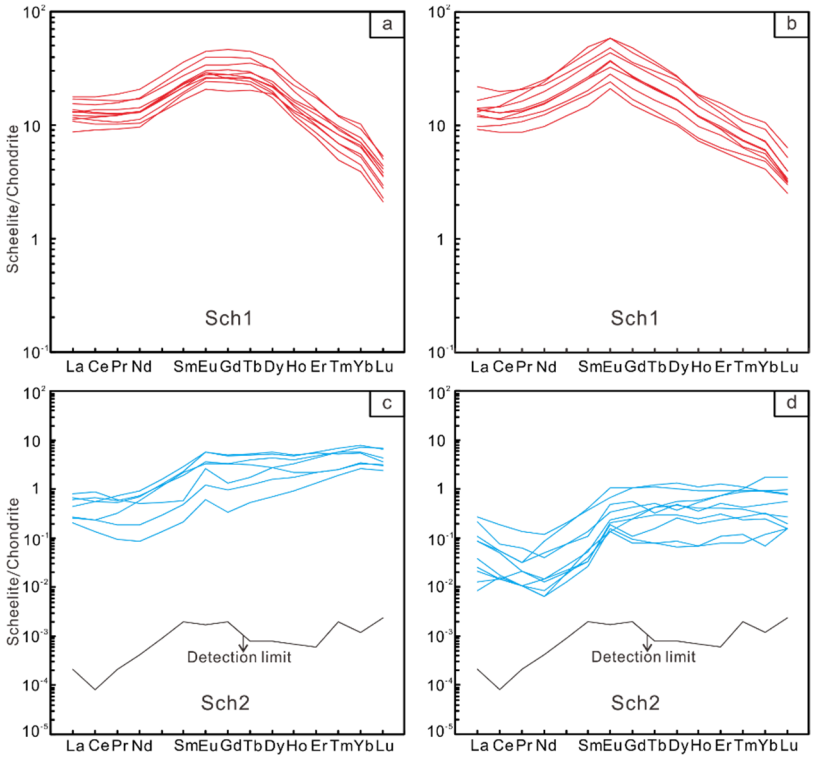

Figure 9. Chondrite-normalized REE patterns of scheelite from the Longshan Sb-Au deposit. (**a**,**b**) Sch1 samples; (**c**,**d**) Sch2 samples. The normalization values are from Sun and McDonough [57].

Sch1 and Sch2 have elevated Sr concentrations (2687 to 6318 ppm and 4525 to 11,040 ppm, respectively) and very low Na and Mo concentrations. The Na and Mo concentrations in Sch1 range from below detection limit (bdl) to 1.64 ppm and 0.004 to 0.017 ppm, respectively. The Na and Mo concentrations in Sch2 range from bdl to 13.1 ppm and 0.014 to 0.648 ppm, respectively. The Rb contents of the Sch1 and Sch2 scheelite samples are bdl, a feature that is consistent with the crystal chemistry of scheelite (less than 3 ppm Rb, [26]).

4.2. Sm-Nd and Sr Isotope Results for the Scheelite

The Sm-Nd concentration and isotope data for scheelites from the Longshan deposit are presented in Table S3. The four Sch1 samples show variations in Sm (3.90 to 20.3 ppm) and Nd (6.24 to 15.4 ppm) concentrations. The $^{147}Sm/^{144}Nd$ ratios of Sch1 range from 0.317 to 0.799, and present-day $^{143}Nd/^{144}Nd$ ratios range from 0.512459 to 0.513120. The Sch1 samples define an excellent linear array with an MSWD =1.0, yielding an age of 210 ± 2 Ma, with an initial ratio of 0.512025 ± 0.000006 (Figure 10). The Sm (0.683 to 11.9 ppm) and Nd (1.01 to 13 ppm) concentrations of the Sch2 samples are highly variable. The $^{147}Sm/^{144}Nd$ ratios of Sch2 range from 0.410 to 0.554, and present-day $^{143}Nd/^{144}Nd$ ratios range from 0.512384 to 0.512907.

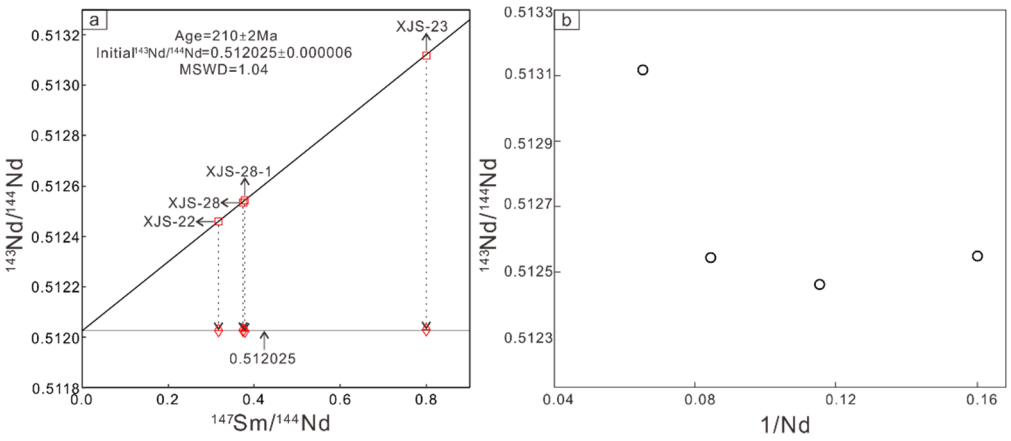

Figure 10. (**a**) Sm-Nd isochron data (□) and initial $^{143}Nd/^{144}Nd$ values at an age of 210 Ma (◊) and (**b**) $^{143}Nd/^{144}Nd$-1/Nd plots (○) of Sch1 samples from the Longshan Sb-Au deposit.

The calculated initial $^{143}Nd/^{144}Nd$ values at an age of 210 Ma for Sch1 are narrow variation (0.512022 to 0.512027, Table S3), with εNd(t) ranging from −6.65 to −6.75. While the initial $^{143}Nd/^{144}Nd$ values for the Sch2 are variable (0.511632 to 0.512208). This variation is also reflected in the εNd(t) values, which range from −3.12 to −14.4. The $^{87}Sr/^{86}Sr$ ratios determined for the Sch1 are rather uniform and range from 0.7209 to 0.7210, with an average value of 0.7209. In contrast, the $^{87}Sr/^{86}Sr$ ratios of Sch2 range widely from 0.7209 to 0.7228, with an average value of 0.7214. The $^{87}Sr/^{86}Sr$ ratios of Sch2 are higher than that of Sch1 while lower than $(^{87}Sr/^{86}Sr)(t)$ of the basement slates in the Banxi Group (0.7430 to 0.7494, average of 0.7467, [12]).

4.3. Sulfur Isotopes

The $\delta^{34}S$ values of the arsenopyrite and pyrite from Stage-3 are −1.8‰ to 0.2‰ and 1.6‰, respectively (Table S4). The $\delta^{34}S$ values of three arsenopyrite grains from Stage-4 range from 2.7‰ to 3.2‰ (Table S4).

5. Discussion

5.1. Timing of Sb-Au Mineralization

A linear array on an isochron diagram may also be the result of mixing between two discrete end-member compositions with different $^{147}Sm/^{144}Nd$ and $^{143}Nd/^{144}Nd$ ratios [8]. However, the $^{143}Nd/^{144}Nd$ ratios plotted versus their corresponding values of 1/Nd do not indicate an inherited collinearity (Figure 10b). Considering that all Sch1 samples were collected from the same ore vein and should be regarded as products of the same hydrothermal event, the scheelite is chemically homogeneous (Figure 8) and the variation range of the calculated εNd(t) for Sch1 is relatively narrow (Table S3). The calculated initial $^{143}Nd/^{144}Nd$ values at an age of 210 Ma for Sch1 are the same within error as the initial $^{143}Nd/^{144}Nd$ value of the isochron (Figure 10a). These features suggest that all Sch1 samples had the same initial isotope ratios of daughter isotopes, and the scheelite Sm-Nd isochron age can be regarded as a single Sch1 hydrothermal event. The high-grade ore of the Sch1 and stibnite vein (Figure 5e) is 25.2 wt. % Sb, 0.23 g/t Au and 13 wt. % W from Stage-3. The mineral assemblage consists of quartz, scheelite, and stibnite. Thus, we believe that the isochron age of 210 ± 2 Ma (Figure 10a) represents the age of the Sb-Au mineralization in the Longshan deposit.

As noted above, many low-temperature Sb-Au deposits are hosted in the Proterozoic metamorphosed clastic rocks in the XZMP (Figure 1b). The Chanziping and Daping gold deposits (Figure 1b) have Rb-Sr isochron dates for fluid inclusions trapped in quartz yielding 205.6 ± 9.4 Ma and 204.8 ± 6.3 Ma, respectively [58]. Scheelite coexisting with stibnite from the Zhazixi Sb-W deposit yielded Sm-Nd isochron ages of 227.3 ± 6.2 Ma [59]. Mineralized granite and granite porphyry yielded

K-Ar dates of 209 Ma for the Fuzhuxi Sb-Au, 200 Ma for the Liaojiaping Sb-Au, and 194–204 Ma for the Banxi Sb deposits [28]. These dates show that there was a widespread multi-commodity W-Sb-Au mineralizing event in the XZMP ca. 210 Ma, which was coeval with the Late Triassic granites (201–228 Ma) in the XZMP [29].

5.2. Genesis of the Longshan Sb-Au Deposit

Due to their similar electronic configurations, ionic radii, and valence states, Mo enters the scheelite lattice as Mo^{6+} by substituting for W^{6+} under oxidizing conditions. With changing redox conditions, more Mo^{6+} is reduced to Mo^{4+} and precipitates as MoS_2 in the fluid under reduced conditions [15,60]. As shown in Figure 11a, the Mo concentrations of our samples are much lower than those of the scheelites from skarn- and porphyry-type W deposits and Au-W deposits [1,4,15,16,50,61]. Further, the precipitation of Stage-4 native antimony (Figure 7i) in the Longshan Sb-Au deposit reflects ore formed under reduced conditions [62]. This interpretation means the ore-forming fluids were relatively reduced.

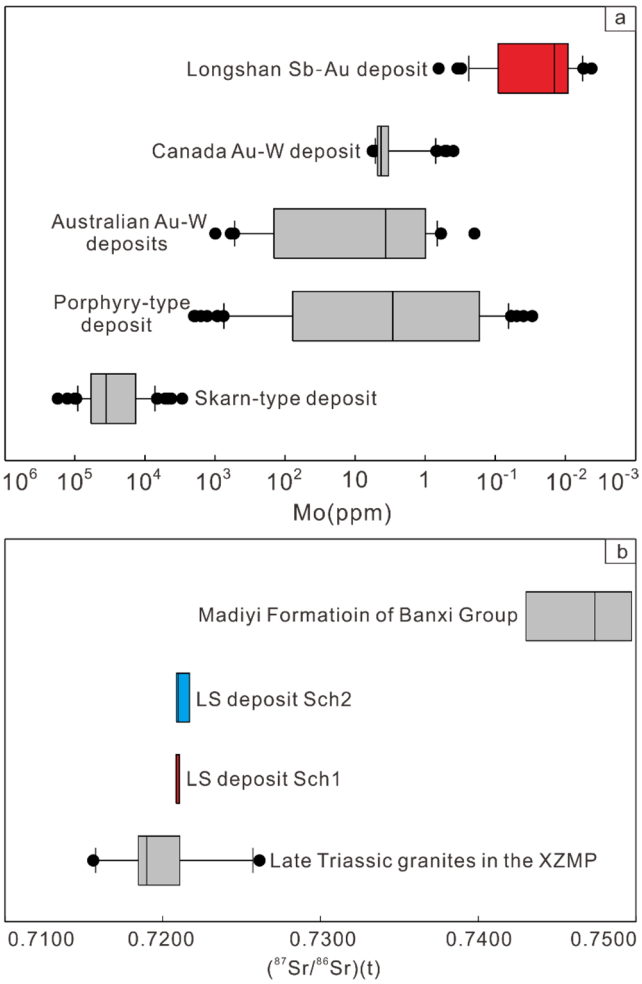

Figure 11. (**a**) Comparison of Mo content (ppm) in scheelite from different type of deposits; (**b**) Plot of $^{87}Sr/^{86}Sr$ ratios for scheelite from the from the Longshan Sb-Au deposit, South China. The ($^{87}Sr/^{86}Sr$) (t = 210 Ma) ratios for Late Triassic granites are from Gao et al. [41]. The ($^{87}Sr/^{86}Sr$)(t = 210 Ma) ratios for Banxi Group basement strata are from Peng and Frei [12].

The different hydrothermal fluids that precipitated scheelite can potentially be distinguished in the LREE-MREE-HREE ternary diagram (Figure 12). Geochemical differences between REE for Sch1 and Sch2 indicate genetic similarities to porphyry- and skarn-type W deposits and quartz vein Au-W

deposits, respectively [1,4,15,16,50,61,63]. Considering that the Sm-Nd age and narrow $^{87}Sr/^{86}Sr$ ratios of Sch1 (Table S3) compare well with those of the Late Triassic granites (Figure 11b, [41]), we interpret Sch1 as a possible precipitate from the primitive ore-forming fluids derived from the Late Triassic granitic intrusion in the XZMP.

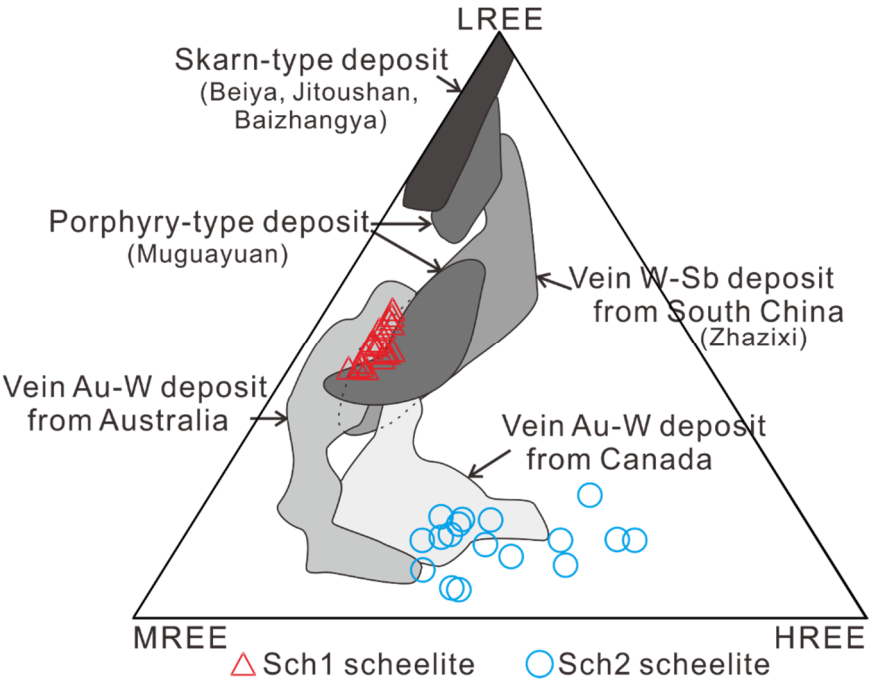

Figure 12. Triangular LREE-MREE-HREE diagram of the scheelite from the Longshan Sb-Au deposit. The REE data of other scheelite from skarn-type deposits, porphyry-type deposit, vein W-Sb deposit, and vein Au-W deposits are from Song et al. [15] and Fu et al. [61]; Li et al. [63]; Peng et al. [50]; Ghaderi et al. [1], Brugger et al. [16], and Dostal et al. [4].

The evolution of the ore-forming fluid can be reflected by compositional changes in scheelite [16,18,64,65]. In the present study, Sch1 in the Longshan deposit has higher REE and lower Sr concentrations than Sch2 (Table 2, Figure 9), indicating that the early fluids were likely characterized by high REE and low Sr contents. The decrease in REE in Sch2 was likely caused by the precipitation of Sch1 and the resulting decrease in REE in the fluid. However, Sch2 has higher Sr concentrations than Sch1 (Table 2, Figure 9). Strontium is compatible in scheelite [16], meaning that the precipitation of Sch1 would have decreased rather than increased the Sr content in fluid. Differentiation of magma cannot elevate the Sr content of exsolved fluids [66,67]. Therefore, an extra source of Sr is required to account for the formation of Sr-enriched Sch2. Sr-enriched scheelite (1455–6810 ppm, [68]) is also analyzed in the Woxi W-Sb-Au deposit (Figure 1b), where high-Sr fluid is thought to have resulted from the hydrothermal leaching of Proterozoic clastic rocks [68]. The basement sequences in the Longshan region are mainly part of the Neoproterozoic Banxi and volcanic and pyroclastic rocks are Sr-enriched (302 to 942 ppm, [69]) and possibly provided the extra Lengjiaxi groups that contain pyroclastic and tholeiitic to calc-alkaline volcanic rocks [36,37,69]. These mafic-intermediate Sr in the Sch2 through fluid-rock interaction. The extra Sr from the basement strata may also be characterized by the Sr isotopic signatures of Sch2. The higher $^{87}Sr/^{86}Sr$ ratios of Sch2 (Table S3, Figure 11b) indicate that the fluids were affected by contamination of radiogenic ^{87}Sr-enriched strata of the Banxi Group during intense wall rock alteration [12,68]. The similar evolving fluids system has been reported from the Woxi W-Sb-Au deposit in the XZMP [12]. In addition, native gold filling in the pyrite (Figure 7e) and arsenopyrite hosted in the altered host rock also suggest that the fluid-rock interaction caused Au precipitation [18].

The restricted range of $\delta^{34}S$ values (−1.8‰ to 3.2‰) (n = 7, Figure 13, Table S4) is similar to that of sulfides in granitic rocks worldwide ($\delta^{34}S$ = +1.0 ± 6.1‰) [70], suggesting a magmatic source for the sulfur. The concentrations of Au in the Neoproterozoic strata are 3.6 ppb in the Lengjiaxi Group and 3.1 ppb in the Banxi Group. These values are only slightly higher than the concentrations of Au in the upper continental crust (1.5 ppb, [71]). The Neoproterozoic strata are unlikely to be the dominant source of Au. In the Longshan deposit, the measured Au concentration in sedimentary pyrite are 1.81–3.46 ppm (unpublished data) and no free gold is observed within sedimentary pyrite. The occurrence of native gold and the high concentration of invisible gold in the pyrite (147–350 ppm, unpublished data) in Stage-3 suggest the late input of Au-rich fluid. The granitic dikes developed around the eastern part of the Longshan dome (Figure 2) also have a higher concentration of Sb (27.2–41.9) ppm [52] than that of Sb (0.4 ppm) in the upper continental crust [71]. Based on the in-situ trace element compositions, Sm-Nd isotope dating of scheelite and the S isotope of sulfides, we infer that Longshan is an intrusion-related Sb-Au deposit associated with the emplacement of the Late Triassic granitic intrusion in the XZMP.

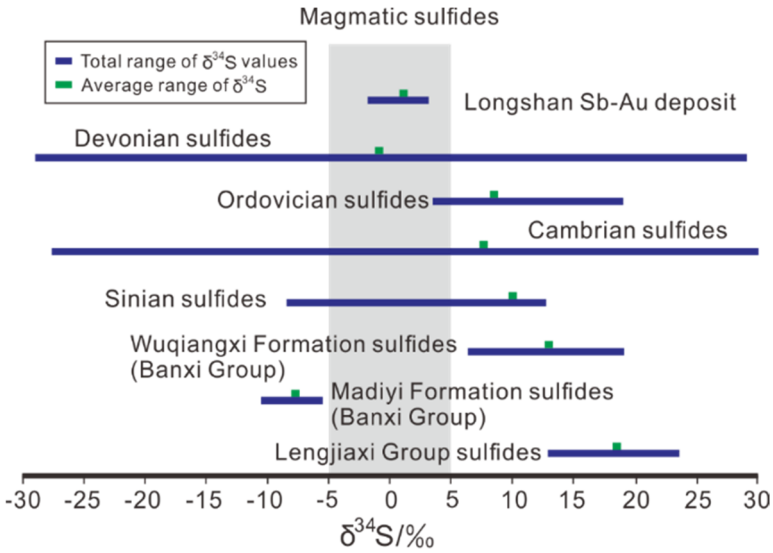

Figure 13. Sulfur isotope composition from the Longshan Sb-Au deposit, South China (Stratum sulfur isotope compositions data are from Hu et al. [28]).

6. Conclusions

(1) The Longshan Sb-Au deposit formed ca. 210 ± 2 Ma, which was coeval with the Late Triassic granites in the XZMP (201–228 Ma). The ages and sulfur isotope indicated that Longshan might be an intrusion-related Sb-Au deposit.

(2) The are two types of scheelite that can be distinguished (Sch1 and Sch2) in the Longshan Sb-Au deposit. Sch1 exhibits high ΣREE + Y contents, low Sr values and a narrow range of $^{87}Sr/^{86}Sr$ values, while Sch2 shows low ΣREE + Y contents, elevated Sr abundance and wide $^{87}Sr/^{86}Sr$ ratios. The basement rocks may provide the extra Sr and radiogenic ^{87}Sr in Sch2 through fluid-rock interaction.

Supplementary Materials: The following are available online at http://www.mdpi.com/2075-163X/9/2/87/s1, Table S1: Sample information from the Longshan Sb-Au deposit, South China, Table S2: Average minimum detection limits and dwell time for scheelite LA-ICP-MS spot analyses from the Longshan Sb-Au deposit, South China, Table S3: Results of scheelite Sm-Nd and Sr isotopic analysis from the Longshan Sb-Au deposit, South China, Table S4: Sulfur isotope composition of sulfides from the Longshan Sb-Au deposit, South China.

Author Contributions: Z.Z. contributed significantly to the data analyses and wrote the manuscript. G.X. and J.M. conceived and designed the experiment and study design. W.L. and P.O. helped perform the analysis with construction discussions. W.L. helped perform the literature search and provided many helpful suggestions about the article.

Funding: National Basic Research Program of China (973 Program, 2014CB440902), National Natural Science Foundation of China (No. 41573042).

Acknowledgments: This research was financially supported by the National Basic Research Program of China (973 Program, 2014CB440902) and the National Natural Science Foundation of China (No. 41573042). The first author thanks the China Scholarship Council (201708110218). We thank the Hunan Xinlong Mining Co., Ltd. and 304 Brigade, the Bureau of Geology for Nuclear Industry of Hunan Province for their kind support in the fieldwork for this study. We also thank Hongying Zhou, Karsten Goemann, Sandrin Feig, Jay Thompson, and Ivan Belousova for their assistance during analysis.

Conflicts of Interest: The authors declare no conflicts of interest.

References

1. Ghaderi, M.J.; Palin, M.; Campbell, I.H.; Sylvester, P.J. Rare earth systematic in scheelite from hydrothermal gold deposits in the Kalgoolie-Norseman Region, Western Australia. *Econ. Geol.* **1999**, *94*, 423–438. [CrossRef]
2. Thompson, J.F.H.; Sillitoe, R.H.; Baker, T.; Land, J.R.; Mortensen, J. Intrusion-related gold deposits associated with tungsten-tin provinces. *Miner. Depos.* **1999**, *34*, 323–334. [CrossRef]
3. Voicu, G.; Bardoux, M.; Stevenson, R.; Jebrak, M. Nd and Sr isotope study of hydrothermal scheelite and host rocks at Omai, Guiana Shield: Implications for ore fluid source and flow path during the formation of orogenic gold deposits. *Miner. Depos.* **2000**, *35*, 302–314. [CrossRef]
4. Dostal, J.; Kontak, D.J.; Chatterjee, A.K. Trace element geochemistry of scheelite and rutile from metaturbidite-hosted quartz vein gold deposits, Meguma Terrane, Nova Scotia, Canada: Genetic implications. *Mineral. Petrol.* **2009**, *97*, 95–109. [CrossRef]
5. Hazarika, P.; Mishra, B.; Pruseth, K.L. Scheelite, apatite, calcite and tourmaline compositions from the late Archean Hutti orogenic gold deposit: Implications for analogous two stage ore fluids. *Ore Geol. Rev.* **2016**, *72*, 989–1003. [CrossRef]
6. Cave, B.J.; Pitcairn, I.K.; Craw, D.; Large, R.R.; Thompson, J.M.; Johnson, S.C. A metamorphic mineral source for tungsten in the turbidite-hosted orogenic gold deposits of the Otago Schist, New Zealand. *Miner. Depos.* **2017**, *52*, 515–537.
7. Bell, K.; Anglin, C.D.; Franklin, J.M. Sm-Nd and Rb-Sr isotope systematics of scheelites: Possible implications for the age and genesis of vein-hosted gold deposits. *Geology* **1989**, *17*, 500–504. [CrossRef]
8. Anglin, C.D.; Jonasson, I.R.; Franklin, J.M. Sm-Nd dating of scheelite and tourmaline: Implications for the genesis of Archean gold deposits, Vald'Or, Canada. *Econ. Geol.* **1996**, *91*, 1372–1382. [CrossRef]
9. Darbyshire, D.P.F.; Pitfield, P.E.J.; Campbell, S.D.G. Late Archean and Early Proterozoic gold-tungsten mineralization in the Zimbabwe Archean craton: Rb-Sr and Sm-Nd isotope constraints. *Geology* **1996**, *24*, 19–22. [CrossRef]
10. Kempe, U.; Belyatsky, B.V.; Krymsky, R.S.; Kremenetsky, A.A.; Ivanov, P.A. Sm-Nd and Sr isotope systematics of scheelite from the giant Au (-W) deposit Muruntau (Uzbekistan): Implications for the age and sources of Au mineralization. *Miner. Depos.* **2001**, *36*, 379–392. [CrossRef]
11. Peng, J.T.; Hu, R.Z.; Zhao, J.H.; Fu, Y.Z.; Lin, Y.X. Scheelite Sm-Nd dating and quartz Ar-Ar dating for Woxi Au-Sb-W deposit, western Hunan. *Chin. Sci. Bull.* **2003**, *48*, 2640–2646. [CrossRef]
12. Peng, B.; Frei, R. Nd-Sr-Pb isotopic constraints on metal and fluid sources in W-Sb-Au mineralization at Woxi and Liaojiaping (Western Hunan, China). *Miner. Depos.* **2004**, *39*, 313–327. [CrossRef]
13. Roberts, S.; Palmer, M.R.; Waller, L. Sm-Nd and REE characteristics of tourmaline and scheelite from the Björkdal gold deposit, northern Sweden: Evidence of an intrusion-related gold deposit. *Econ. Geol.* **2006**, *101*, 1415–1425. [CrossRef]
14. Raimbault, L.; Baumer, A.; Dubru, M.; Benkerrou, C.; Croze, V.; Zahm, A. REE fractionation between scheelite and apatite in hydrothermal conditions. *Am. Mineral.* **1993**, *78*, 1275–1285.
15. Song, G.X.; Qin, K.Z.; Li, G.M.; Evans, N.J.; Chen, L. Scheelite elemental and isotopic signatures: Implications for the genesis of skarn-type W-Mo deposits in the Chizhou area, Anhui Province, eastern China. *Am. Mineral.* **2014**, *99*, 303–317. [CrossRef]
16. Brugger, J.; Bettiol, A.A.; Costa, S.; Lahaye, Y.; Bateman, R.; Lambert, D.D.; Jamieson, D.N. Mapping REE distribution in scheelite using luminescence. *Mineral. Mag.* **2000**, *64*, 891–903. [CrossRef]

17. Brugger, J.; Mass, R.; Lahaye, Y.; McRae, C.; Ghaderi, M.; Costa, S.; Lambert, D.; Bateman, R.; Prince, K. Origins of Nd-Sr-Pb isotopic variations in single scheelite grains from Archaean gold deposits, Western Australia. *Chem. Geol.* **2002**, *182*, 203–225. [CrossRef]
18. Brugger, J.; Etschmann, B.; Pownceby, M.; Liu, W.H.; Grundler, P.; Brewe, D. Oxidation state of europium in scheelite: Tracking fluid-rock interaction in gold deposits. *Chem. Geol.* **2008**, *257*, 26–33. [CrossRef]
19. Brugger, J.; Lahaye, Y.; Costa, S.; Lambert, D.; Bateman, R. Inhomogeneous distribution of REE in scheelite and dynamics of Archaean hydrothermal systems (Mt. Charlotte and Drysdale gold deposits, Western Australia). *Contrib. Mineral. Petrol.* **2000**, *139*, 251–264. [CrossRef]
20. Ding, T.; Ma, D.S.; Lu, J.J.; Zhang, R.Q. Garnet and scheelite as indicators of multi-stage tungsten mineralization in the Huangshaping deposit, southern Hunan province, China. *Ore Geol. Rev.* **2018**, *94*, 193–211. [CrossRef]
21. Zhao, W.W.; Zhou, M.F.; Williams-Jones, A.E.; Zhao, Z. Constraints on the uptake of REE by scheelite in the Baoshan tungsten skarn deposit, South China. *Chem. Geol.* **2018**, *477*, 123–136. [CrossRef]
22. Uspensky, E.; Brugger, J.; Graeser, S. REE geochemistry systematics of scheelite from the Alps using luminescence spectroscopy: From global regularities to local control. Schweiz. *Mineral. Petrogr. Mitt.* **1998**, *78*, 31–54.
23. Poulin, R.S.; Mcdonald, A.M.; Kontak, D.J.; Mcclenaghan, M.B. On the relationship between cathodoluminescence and the chemical composition of scheelite from geologically diverse ore-deposit environments. *Can. Mineral.* **2016**, *54*, 1147–1173. [CrossRef]
24. Poulin, R.S.; Kontak, D.J.; Mcdonald, A. Assessing scheelite as an ore-deposit discriminator using its trace-element and REE chemistry. *Can. Mineral.* **2018**, *56*, 265–302. [CrossRef]
25. Deer, W.A.; Howie, R.A.; Zussman, J. *An Introduction to the Rock Forming Minerals*; Longman Press: New York, NY, USA, 1966; p. 515.
26. Eichhorn, R.; Holl, R.; Jagoutz, E.; Scharer, U. Dating scheelite stages: A strontium, neodymium, lead approach from the felbertal tungsten deposit, Central Alps, Austria. *Geochim. Cosmochim. Acta* **1997**, *61*, 5005–5022. [CrossRef]
27. Scanlan, E.J.; Scott, J.M.; Wilson, V.J.; StiRLING, C.H.; Reid, M.R.; Roux, P.J. In suit $^{87}Sr/^{86}Sr$ of scheelite and calcite reveals proximal and distal fluid-rock interaction during orogenic W-Au mineralization, Otago Schist, New Zealand. *Econ. Geol.* **2018**, *113*, 1571–1586. [CrossRef]
28. Hu, R.Z.; Fu, S.L.; Huang, Y.; Xiao, J.F. The giant South China Mesozoic low-temperature metallogenic domain: Reviews and a new geodynamic model. *J. Asian Earth Sci.* **2017**, *137*, 9–34. [CrossRef]
29. Xie, G.Q.; Mao, J.W.; Bagas, L.; Fu, B.; Zhang, Z.Y. Mineralogy and titanite geochronology of the Caojiaba W deposit, Xiangzhong metallogenic province, southern China: Implications for a distal reduced skarn W formation. *Miner. Depos.* **2018**. [CrossRef]
30. Gu, X.X.; Schulz, O.; Vavtar, F.; Liu, J.M.; Zheng, H.; Fu, S.H. Rare earth element geochemistry of the Woxi W-Sb-Au deposit, Hunan Province, South China. *Ore Geol. Rev.* **2007**, *31*, 319–336. [CrossRef]
31. Zhu, Y.N.; Peng, J.T. Infrared microthermometric and noble gas isotope study of fluid inclusions in ore minerals at the Woxi orogenic Au-Sb-W deposit, western Hunan, South China. *Ore Geol. Rev.* **2015**, *65*, 55–69. [CrossRef]
32. *Geological Map of Hunan Province, the People's Republic of China 1:500,000*; Geological Publishing House: Beijing, China, 2010. (In Chinese)
33. Chu, Y.; Lin, W.; Faure, M.; Wang, Q.; Ji, W. Phanerozoic tectonothermal events of the Xuefengshan Belt, 548 central South China: Implications from U-Pb age and Lu-Hf determinations of granites. *Lithos* **2012**, *150*, 243–255. [CrossRef]
34. Shi, M.K.; Fu, B.Q.; Le, X.X.; Zhou, X.C. *Antimony Metallogeny in Central Part of Hunan Province*; Hunan Science and Technology Press: Changsha, China, 1993; pp. 1–151.
35. Fu, S.L.; Hu, R.Z.; Chen, Y.W.; Luo, J.C. Chronology of the Longshan Au-Sb deposit in central Hunan Province: Constraints from pyrite Re-Os and zircon U-Th/He isotopic dating. *Acta Petrol. Sin.* **2016**, *32*, 3507–3517.
36. Wang, X.C.; Li, X.H.; Li, W.X.; Li, Z.X. Ca. 825 Ma komatiitic basalts in South China: First evidence for >1500 °C mantle melts by a Rodinian mantle plume. *Geology* **2007**, *35*, 1103–1106. [CrossRef]

37. Wang, X.L.; Zhou, J.C.; Griffin, W.L.; Wang, R.C.; Qiu, J.S.; O'Reily, S.Y.; Xu, X.S.; Liu, X.M.; Zhang, G.L. Detrital zircon geochronology of Precambrian basement sequences in the Jiangnan Orogen: Dating the assembly of the Yangtze and Cathaysia Blocks. *Precambrian Res.* **2007**, *159*, 117–131. [CrossRef]
38. Ma, D.S.; Pan, J.Y.; Xie, Q.L.; He, J. Ore source of Sb (Au) deposits in center Hunan: I. evidences of trace elements and experimental geochemistry. *Miner. Depos.* **2002**, *3*, 366–376.
39. Wang, Y.J.; Fan, W.M.; Sun, M.; Liang, X.Q.; Zhang, Y.H.; Peng, T.P. Geochronlogical, geochemical and geothermal constraints on petrogenesis of the Indosinian peraluminous granites in the South China Block: A case study in Hunan province. *Lithos* **2007**, *96*, 475–502. [CrossRef]
40. Fu, S.L.; Hu, R.Z.; Bi, X.W.; Chen, Y.W.; Yang, J.H.; Huang, Y. Origin of Triassic granites in central Hunan 576 province, South China: Constraints for zircon U-Pb ages and Hf-O isotopes. *Int. Geol. Rev.* **2015**, *57*, 97–111. [CrossRef]
41. Gao, P.; Zheng, Y.F.; Zhao, Z.F. Triassic granites in South China: A geochemical perspective on their characteristics, petrogenesis, and tectonic significance. *Earth Sci. Rev.* **2017**, *173*, 266–294. [CrossRef]
42. Xie, G.Q.; Mao, J.W.; Li, W.; Fu, B.; Zhang, Z.Y. Granite-related Yangjiashan tungsten deposit, southern China. *Miner. Depos.* **2018**. [CrossRef]
43. Rao, J.R.; Wang, J.H.; Cao, Y.Z. Deep structure in Hunan. *Hunan Geol.* **1993**, *12*, 1–101.
44. Hu, R.Z.; Zhou, M.F. Multiple Mesozoic mineralization events in South China—An introduction to the thematic issue. *Miner. Depos.* **2012**, *47*, 579–588. [CrossRef]
45. Mao, J.W.; Cheng, Y.B.; Chen, M.H.; Pirajno, F. Major types and time-space distribution of Mesozoic ore deposits in South China and their geodynamic settings. *Miner. Depos.* **2013**, *48*, 267–294.
46. Li, H.; Wu, Q.H.; Evans, N.J.; Zhou, Z.K.; Kong, H.; Xi, X.S.; Lin, Z.W. Geochemistry and geochronology of the Banxi Sb deposit: Implications for fluid origin and the evolution of Sb mineralization in central-western Hunan, South China. *Gondwana Res.* **2018**, *55*, 112–134. [CrossRef]
47. Peng, B.; Piestrzynski, A.; Chen, G.H. Super-pure native gold in W-Sb-Au ores from the Woxi deposit in western Hunan province, China. *Geotecton. Metal.* **2000**, *24*, 51–56.
48. Peng, B.; Chen, G.H.; Piestrzynski, A. Ore mineralogy of the massive stibnite ore-veins and its genetic implication for the Woxi deposit in western Hunan, China. *Acta Mineral. Sin.* **2003**, *23*, 82–90.
49. Peng, B.; Frei, R.; Tu, X.L. Nd-Sr-Pb isotopic geochemistry of scheelite from the Woxi W-Sb-Au deposit, Western Hunan: Implications for sources and evolution of ore-forming fluids. *Acta Geol. Sin.* **2006**, *80*, 561–570.
50. Peng, J.T.; Zhang, D.L.; Hu, R.Z.; Wu, M.J.; Liu, X.M.; Qi, L.; Yu, Y.G. Inhomogeneous distribution of rare earth elements (REEs) in scheelite from the Zhazixi W-Sb deposit, western Hunan and its geological implications. *Geol. Rev.* **2010**, *56*, 810–819.
51. Peng, J.T.; Hu, R.Z.; Burnard, P.G. Samarium-neodymium isotope systematics of hydrothermal calcites from the Xikuangshan antimony deposit (Hunan, China): The potential of calcite as a geochronometer. *Chem. Geol.* **2003**, *200*, 129–136. [CrossRef]
52. Chen, Y.W.; Bi, X.W.; Fu, S.L.; Dong, S.H. Zircon U-Pb dating and Hf isotope of the felsic dykes in the Longshan Au-Sb deposit in Central Hunan Province and their geological significance. *Acta Petrol. Sin.* **2016**, *32*, 3469–3488.
53. Hunan Bureau of Geology & Mineral Resources (HBGMR). *Report of Resource Substitution Exploration in the Longshan Deposit, Xinshao County, Hunan Province*; Hunan Bureau of Geology & Mineral Resources (HBGMR): Yueyang, China, 2011; pp. 1–94.
54. Weis, D.; Kieffer, B.; Maerschalk, C.; Barling, J.; Jong, J.; Williams, G.A.; Hanano, D.; Pretorius, W.; Mattirlli, N.; Scoates, J.S.; et al. High-precision isotopic characterization of USGS reference materials by TIMS and MC-ICP-MS. Geochem. *Geophys. Geosyst.* **2006**, *7*. [CrossRef]
55. Ludwig, K.R. *Isoplot 3.0–A Geochronological Toolkit for Microsoft Excel*; Berkeley Geochronology Center Special Publication: Berkeley, CA, USA, 2003; Volume 4, pp. 1–70.
56. Steiger, R.H.; Jäger, E. Subcommission on geochronology: Convention on the use of decay constants in geo- and cosmo-chronology. *Earth Planet. Sci. Lett.* **1977**, *36*, 359–362. [CrossRef]
57. Sun, S.S.; McDonough, W.F. Chemical and isotopic systematics of oceanic basalts: Implications for mantle composition and processes. *Geol. Soc. Lond. Spec. Publ.* **1989**, *42*, 313–345. [CrossRef]
58. Li, H.Q.; Wang, D.H.; Chen, F.W.; Mei, Y.P.; Cai, H. Study on chronology of the Chanziping and Daping gold deposit in Xuefeng Mountains, Hunan Province. *Acta Geol. Sin.* **2008**, *82*, 900–905.

59. Wang, Y.L.; Chen, Y.C.; Wang, D.H.; Xu, J.; Chen, Z.H. Scheelite Sm-Nd dating of the Zhazixi W-Sb deposit in Hunan and its geological significance. *Geol. China* **2012**, *39*, 1339–1344.
60. Linnen, R.L.; Williams-Jones, A.E. Evolution of aqueous-carbonic fluids during contact metamorphism, wall-rock alteration, and molybdenite deposition at Trout Lake, British Columbia. *Econ. Geol.* **1990**, *85*, 1840–1856. [CrossRef]
61. Fu, Y.; Sun, X.M.; Zhou, H.Y.; Lin, H.; Jiang, L.Y.; Yang, T.J. In-situ LA-ICP-MS trace elements analysis of scheelites from the giant Beiya gold-polymetallic deposit in Yunnan Province, Southwest China and its metallogenic implications. *Ore Geol. Rev.* **2017**, *80*, 828–837. [CrossRef]
62. An, F.; Zhu, Y.F. Native antimony in the Baogutu gold deposit (west Junggar, NW China): Its occurrence and origin. *Ore Geol. Rev.* **2010**, *37*, 214–223. [CrossRef]
63. Li, X.Y.; Gao, J.F.; Zhang, R.Q.; Lu, J.J.; Chen, W.H.; Wu, J.W. Origin of the Muguayuan veinlet-disseminated tungsten deposit, South China: Constraints from in-situ trace element analyses of scheelite. *Ore Geol. Rev.* **2018**, *99*, 180–194. [CrossRef]
64. Sun, K.K.; Chen, B. Trace elements and Sr-Nd isotopes of scheelite: Implications for the W-Cu-Mo polymetallic mineralization of the Shimensi deposit, South China. *Am. Mineral.* **2017**, *102*, 1114–1128.
65. Zhang, Q.; Zhang, R.Q.; Gao, J.F.; Lu, J.J.; Wu, J.W. In-situ LA-ICP-MS trace elemental analyses of scheelite and wolframite: Constraints on the genesis of veinlet-disseminated and vein-type tungsten deposits, South China. *Ore Geol. Rev.* **2018**, *99*, 166–179. [CrossRef]
66. Bai, T.B.; Groos, A.F.K. The distribution of Na, K, Rb, Sr, Al, Ge, Cu, W, Mo, La, and Ce between granitic melts and coexisting aqueous fluids. *Geochim. Cosmochim. Acta* **1999**, *63*, 1117–1131. [CrossRef]
67. Chappell, B.W.; White, A.J.R. I-type and S-type granites in the Lachlan Fold Belt. *Trans. R. Soc. Edin.* **1992**, *83*, 1–26. [CrossRef]
68. Peng, J.T.; Hu, R.Z.; Zhao, J.H.; Fu, Y.Z.; Yuan, S.D. The ore-forming fluid with a marked radiogenic ^{87}Sr signature from the Woxi Au-Sb-W deposit and its significant implications. *Bull. Mineral. Petrol. Geochem.* **2003**, *22*, 193–196.
69. Wang, X.L.; Zhou, J.C.; Qiu, J.S.; Gao, J.F. Geochemistry of the Meso-to Neoproterozoic basic-acid rocks from Hunan Province, South China: Implications for the evolution of the western Jiangnan orogeny. *Precambrian Res.* **2004**, *133*, 17–103. [CrossRef]
70. Seal, R.R. Sulfur isotope geochemistry of sulfide minerals. *Rev. Mineral. Geochem.* **2006**, *61*, 633–677. [CrossRef]
71. Rudnick, R.L.; Gao, S. Composition of the continental crust. *Treat. Geochem.* **2003**, *3*, 659.